Eng. Sci., 2025, **37**, 1769

Engineered Science
DOI: https://dx.doi.org/10.30919/es1769

Order Matters: Sequential Mechanical Shot Peening/Laser Shock Peening Engineering for A100 Steel Tailors Hydrophobicity-residual Stress Trade-offs

Guoxin Lu,[1,*] Di Zhao,[1] Qiang Wang,[2] Zhong Ji[1] and Zhong Chen[3]

Abstract

This study investigates the synergistic effects of mechanical shot peening (MSP) and laser shock peening (LSP) composite processes on the "wettability functionalization-mechanical strengthening" of A100 steel. By designing MSP-LSP (MSP followed by LSP) and LSP-MSP (LSP followed by MSP) sequences, the regulation mechanisms of hierarchical surface morphology, residual stress distribution, and wettability evolution were elucidated. Laser confocal microscopy revealed that MSP-LSP preserved periodic macro-waviness (1.25×1.25 mm^2 pits) from LSP while enhancing micro-roughness (Sa=1.62±0.04 μm), achieving Cassie-Baxter state via multi-scale coupling. In contrast, LSP-M SP introduced higher residual compressive stress (-1271.93±10.92 MPa) due to secondary hardening but compromised macro-waviness integrity, resulting in lower roughness (*Sa*=1.50±0.08 μm) and contact angle (86.14° vs. 91.58° for MSP-LSP). Finite element simulations confirmed that process sequence governed deformation accumulation: LSP-MSP leveraged stress-gradient-driven non-uniform deformation to amplify residual stress (47.8% increase vs. single processes), while MSP-LSP optimized hierarchical structures for hydrophobicity through waviness-roughness synergy. X-ray diffraction analysis demonstrated that post-treatment dominated microstructural evolution, with LSP-MSP exhibiting higher dislocation density (FWHM=5.61° vs. 5.07° for MSP-LSP). The study establishes a process-sequence-dependent dual-performance optimization strategy: LSP-MSP prioritizes mechanical strengthening, whereas MSP-LSP enhances wettability regulation. These findings provide critical insights into tailoring composite surface engineering for aerospace materials requiring multifunctional integration.

Keywords: Mechanical shot peening (MSP); Laser shock peening (LSP); Surface wettability; Mechanical strengthening; Process sequence effect.
Received: 25 May 2025; Revised: 27 September 2025; Accepted: 29 September 2025
Article type: Research article.

1. Introduction

Mechanical shot peening (MSP)[1] and laser shock peening (LSP),[2] as representative surface modification techniques, hold significant value in optimizing structural material performance. MSP induces work hardening through projectile impacts but suffers from insufficient strengthening depth and nonuniform deformation.[3,4] In contrast, LSP generates deep compressive residual stresses via high-energy laser shockwaves, yet exhibits limited adaptability to components with complex geometries.[5] Recent advancements in hybrid processes highlight synergistic effects—for instance, Kishore *et al*.[6] developed a laser-assisted ultrasonic impact process to achieve directional nanostructuring on metallic surfaces, while Tserpes' team[7] elucidated shockwave propagation mechanisms in multiphase materials through finite element simulations. However, existing studies predominantly focus on individual process mechanisms or simple additive effects, leaving a critical gap in systematically understanding how process sequence governs the "functionalization-strengthening" synergy in composite surface engineering.

Aerospace applications demand multifunctional integration in materials, particularly for ultrahigh-strength steels requiring concurrent fatigue resistance and anti-icing/corrosion properties.[8,9] Conventional single-process

---

[1] *MOE Key Laboratory for Liquid-Solid Structural Evolution and Processing of Materials, Shandong University, Jinan, Shandong, 250061, China*

[2] *Aviation Key Laboratory of Science and Technology on Advanced Corrosion and Protection for Aviation Material, AECC Beijing Institute of Aeronautical Materials, Beijing, 100095, China*

approaches face inherent limitations: MSP enhances hardness but compromises wettability control due to stochastic surface roughness,[10,11] whereas LSP improves hydrophobicity through periodic microstructures but risks surface ablation under localized thermal effects.[12,13] Although composite processes demonstrate potential (*e.g.*, a 9.3-fold improvement in bending fatigue life for titanium alloys via LSP-MSP sequencing[14]), quantitative insights into multiscale morphological evolution, wettability response mechanisms, and sequence-dependent performance boundaries remain scarce. Surface functionalization relies critically on hierarchical architectures regulating wettability: Gou *et al*.[15] achieved a 158° contact angle using LSP-fabricated gradient wavy structures based on the Cassie-Baxter theory, while excessive MSP-induced roughness was shown to degrade wettability.[16,17] Despite the potential of spatially coupled multiscale structures, current research lacks strategies to optimize dual-functional performance (wettability vs. mechanical strengthening) through process sequence engineering.[18,19]

This study systematically investigates the sequence-dependent regulation mechanisms of “wettability-strengthening” duality in A100 steel. By integrating the Fabbro shockwave model[20,21] with 3D dynamic loading simulations, we establish a multiscale framework coupling stochastic MSP impacts and periodic LSP loading. Three key aspects are resolved: (1) The influence of waviness-roughness spatial coupling on Cassie-Baxter wetting states;[22,23] (2) Plastic strain accumulation pathways regulated by process sequence, governing residual stress redistribution; (3) Competitive and synergistic boundaries between functionalization and strengthening. Laser confocal microscopy quantifies surface morphology thresholds, complemented by X-ray diffraction analysis of dislocation density evolution. These findings establish a function-mechanics integrated design paradigm, offering theoretical guidelines and process optimization strategies for advanced structural materials.

2. Experimental

2.1 Materials and post-processing

The study employed A100 ultrahigh-strength steel, a representative aeronautical material, with the following composition (wt%): C (0.21–0.25%), Co (13–14%), Ni (11–12%), Cr (2.9–3.3%), Mo (1.1–1.3%), and trace alloying elements. Rectangular specimens were machined via grinding and subjected to standardized heat treatment to eliminate initial processing variations.

Composite surface treatments combined MSP and LSP in alternating sequences:

MSP parameters: ASH600 projectiles (0.6 mm diameter), Almen intensity 0.2 mmA, 100% surface coverage, full-surface impact trajectory.

LSP parameters: Laser energy 6 J, pulse width 15 ns, spot diameter 2.5 mm, S-shaped scanning path with 50% overlap ratio.

Processing sequences: Two regimens were designed—MSP-LSP (MSP followed by LSP) and LSP-MSP (LSP followed by MSP). Post-treated specimens were sectioned using wire electrical discharge machining for standardized testing.

2.2 Testing and characterization

(1) Surface morphology and roughness analysis

Surface roughness (*Sa*) was quantified using a Karthmatic KC-X1000 laser confocal microscope across two distinct scales: 2.5 × 2.5 mm^2 (single-spot region) and 3.0 × 3.0 mm^2 (1.2× spot-overlap region) (Fig. 1a). Special emphasis was placed on identifying demarcation characteristics between waviness and roughness.

(2) Wettability Testing

A DSA-X optical contact angle analyzer was employed to measure the contact angle of 5 μL deionized water droplets on specimen surfaces using the sessile drop method. Five measurements were performed at different locations per sample (Fig. 1b), with the results averaged to ensure statistical reliability.

(3) Residual Stress Analysis

Surface residual stresses were quantified via the $\sin^2\psi$ method using a Proto LXRD X-ray diffractometer. The sample material exhibited elastic constants of $(1/2)S2 = 5.67\times10^6$ MPa^{-1} and $-S1 = 1.20\times10^6$ MPa^{-1}. The {211} crystal plane family was selected as the diffraction plane. A Cr-Kα radiation source with a 3 mm collimator diameter was utilized. During measurements, the surface normal of the sample served as the reference axis, with ψ angles ranging from 25° to 25° for multi-angle exposures. Five measurements per sample (Fig. 1b) were conducted, and the mean value was adopted as the representative stress.

2.3 Finite element simulation and analysis

A three-dimensional finite element (FE) model was developed in ABAQUS to simulate the laser shock peening process, with dynamic loading conditions programmatically

---

[3] *Jiangsu Key Laboratory of Advanced Manufacturing Technology, Huaiyin Institute of Technology, Huai'an, Jiangsu, 223001, China*
[*] *Email:* gxlu@sdu.edu.cn (Guoxin Lu)

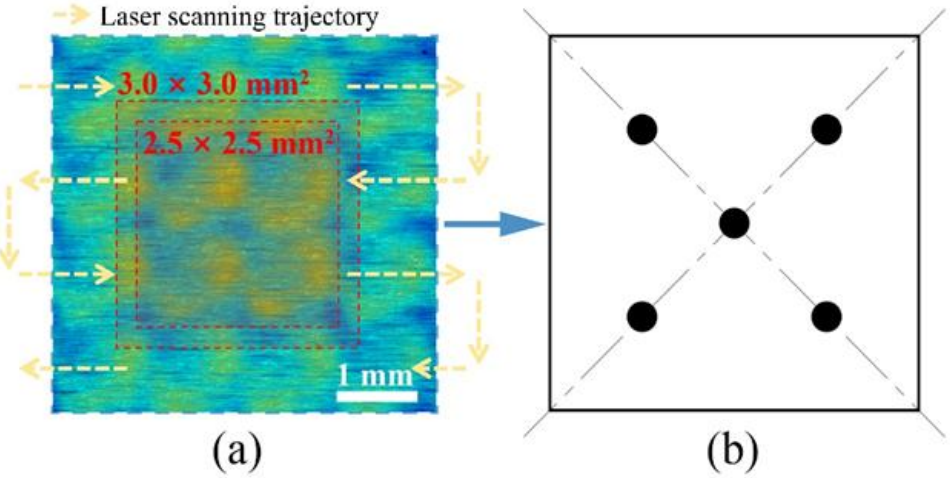

Fig. 1: Schematic diagram of Sampling locations for residual stress, contact angle, and surface roughness measurements. (a) Sampling areas for surface roughness (2.5×2.5 mm^2 and 3.0×3.0 mm^2); (b) Sampling positions for residual stress and contact angle (black dots).

Note: The testing or analysis paths for the surface integrity indicators are identical to the laser beam scanning path in the LSP process.

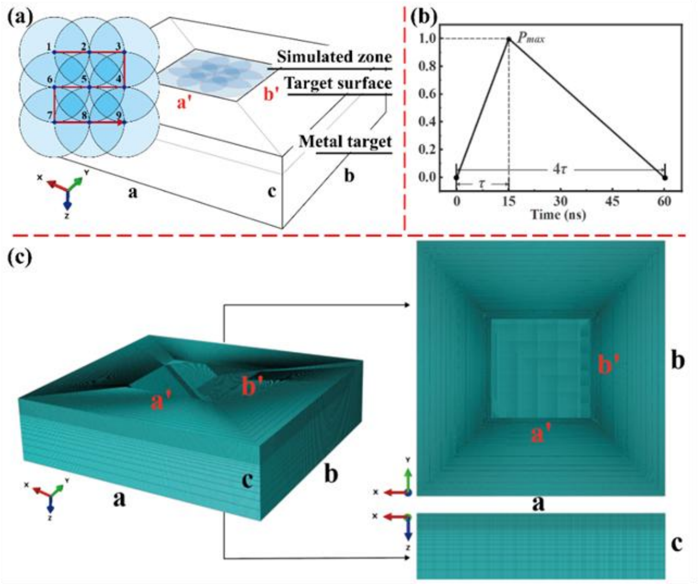

Fig. 2: FE model of the LSP process. (a) Laser shock path and overlap rate (S-shaped trajectory); (b) Simplified triangular waveform of laser shock pressure; (c) Meshing strategy for the target material.

implemented via Fortran.

As illustrated in Fig. 2, the FE model accurately replicates key characteristics of practical LSP operations: The S-shaped laser scanning trajectory with 50% overlap ratio is explicitly reconstructed (Fig. 2a). The model dimensions (15 mm (a) × 15 mm (b)× 4 mm (c)) incorporate a 5 mm (a') × 5 mm (b') laser-impacted zone (blue-highlighted region in Fig. 2a), accounting for 11.1% of the total surface area to minimize boundary effects on simulation accuracy.

For material constitutive modeling, the Johnson-Cook plasticity model[25,26] was selected to capture the strain rate hardening and thermal softening behavior of A100 steel under extreme strain rates (10^6–10^7 s^{-1}).[24] The laser shockwave loading was simplified as a pure pressure pulse based on the Fabbro theoretical framework,[21,27] with spatial pressure distribution following a top-hat profile and temporal evolution approximated as a triangular waveform (Fig. 2b).[28]

A differentiated meshing strategy (Fig. 2c) balanced computational efficiency and resolution: The impact zone employed refined elements to resolve high-stress gradients, while coarser meshes were applied to non-impact regions. Transitional mesh layers were implemented at spot overlap boundaries to ensure stress wave propagation continuity, addressing the periodic nature of laser scanning paths.

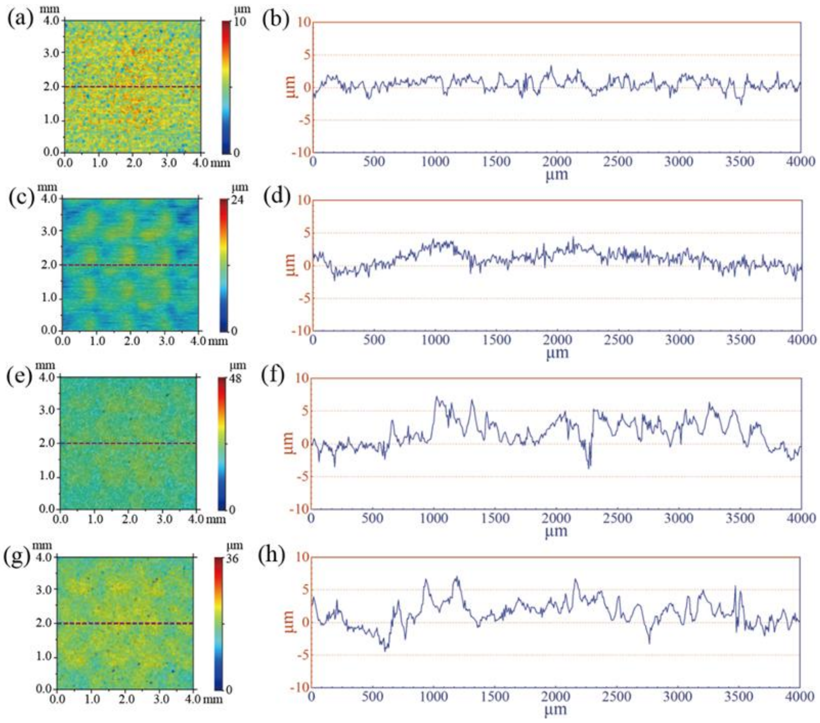

Fig. 3: Laser confocal microscopy images of surface morphology under different post-treatment processes. The laser scanning paths used in the laser shock process are the same as those in (c). (a) MSP-treated surface; (c) LSP-treated surface; (e) MSP-LSP-treated surface; (g) LSP-MSP-treated surface; (b, d, f, h) Comparison of surface disorder between different post-treatments, corresponding to the undulation profiles along the purple dashed lines in (a), (c), (e), and (g), respectively.

It should be noted that input parameters, including the properties of the target material as well as laser spot diameter, pulse pressure, etc., are all set or calculated according to the content in Section 2.1. After completing the finite element simulation involving the LSP process, output parameters such as equivalent plastic strain and residual stress will be specifically analyzed to serve as a foundation and provide support for subsequent discussions on composite post-processing mechanisms.

3. Results

3.1 Surface morphology evolution under different post-processing sequences

Systematic characterization via laser confocal microscopy (Fig. 3) revealed distinct surface modification mechanisms governed by processing sequences. For MSP-only treated specimens (Fig. 3a-b), uniformly distributed projectile indentations dominated the surface morphology. Localized height variations arising from stochastic micropits exhibited continuous gradients, yet lacked pronounced macroscale waviness, resulting in an indistinct demarcation threshold between waviness and roughness.

In contrast, LSP-only processing generated periodic pit arrays with a characteristic 1.25×1.25 mm^2 spatial periodicity (Fig. 3(c-d)). These laser-induced macropits formed alternating concave-convex architectures at the millimeter scale, while subsidiary microstructures within each pit—attributable to shockwave interactions—created a dual-scale hierarchy. This hierarchy manifested as clear distinctions in spatial frequency and amplitude.

Composite processes demonstrated sequence-dependent synergistic effects (Fig. 3(e-h)). Both MSP-LSP and LSP-MSP sequences inherited micron-scale MSP indentations and LSP macropits but diverged in structural evolution pathways. For MSP-LSP (Fig. 3(e-f)), the uniform MSP-treated substrate preserved LSP-induced periodicity, amplifying macrowaviness height while reducing pit width. Concurrently, microroughness amplitude and spatial frequency increased respectively, lowering the waviness-roughness demarcation threshold. Conversely, LSP-MSP specimens (Fig. 3(g-h)) exhibited higher topographical disorder due to MSP-induced erosion of initial LSP macropits. Subsequent MSP impacts reduced macrowaviness prominence while increasing roughness density and dispersion.

Critical analysis of Fig. 3(f-h) highlights the deterministic role of processing sequence in final topography. Post-treatment steps exerted dominant modification effects through cumulative interactions with pre-existing morphologies. Specifically, MSP as a post-treatment (LSP-MSP) disrupted LSP-generated periodicity via stochastic projectile impacts,

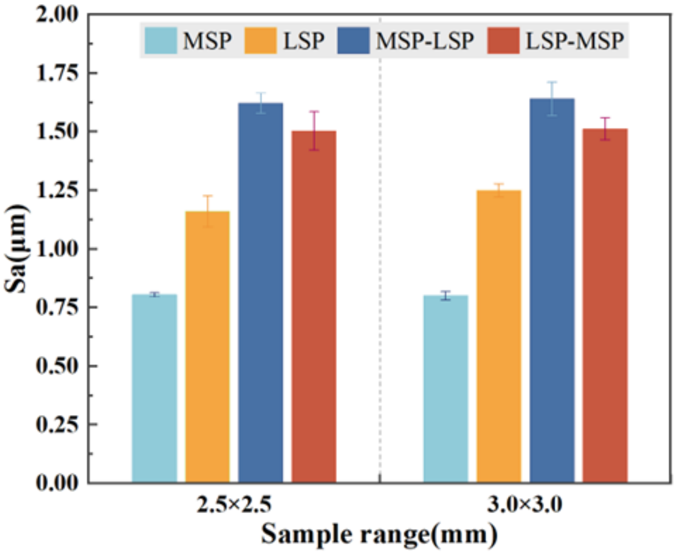

Fig. 4: Comparison of areal surface roughness (*Sa*) under different treatment processes. Results for 2.5×2.5 mm^2 and 3.0×3.0 mm^2 Sampling areas. Error bars represent standard deviations.

whereas LSP as a post-treatment (MSP-LSP) reconstructed enhanced periodicity on the MSP-homogenized substrate through controlled shockwave propagation. This sequence-governed morphological regulation provides direct experimental evidence for the synergy in composite surface engineering.

3.2 Influence of combined impact modification processes on surface roughness

The regulatory effects of processing sequences on surface roughness were systematically evaluated through waviness-roughness demarcation analysis (Fig. 4). A dual-scale sampling strategy was implemented to mitigate measurement interference: areal roughness (*Sa*) measurements were conducted in both the LSP-periodicity-dominated core zone (2.5 × 2.5 mm^2) and the spot-overlap-inclusive extended zone (3.0 × 3.0 mm^2). As shown in Fig. 4, both sampling regimes revealed consistent trends: MSP-only treatment yielded the lowest *Sa* values, followed by LSP-only processing. Among composite processes, LSP-MSP exhibited marginally higher *Sa* (1.50 ± 0.08 μm) than LSP-only, while MSP-LSP achieved the maximum *Sa* (1.62 ± 0.04 μm).

This roughness hierarchy stems from sequence-dependent surface morphology evolution. The periodic pit arrays generated by LSP-only treatment, despite their macroscopic undulations, reduced spatial heterogeneity through ordered arrangements, resulting in lower-than-expected *Sa* values. Conversely, MSP-only processing produced densely distributed stochastic micro-indentations, but the absence of superimposed macrowaviness limited overall *Sa* enhancement. In MSP-LSP specimens (Fig. 3(e-f)), the MSP-pretreated homogeneous substrate facilitated coherent propagation of subsequent LSP shockwaves, preserving periodic pit geometry while amplifying both pit depth and adjacent peak-valley contrasts. This synergistic coupling between macrowaviness and microroughness maximized *Sa* elevation. In contrast, LSP-MSP processing (Fig. 3(g-h)) suffered partial degradation of initial LSP periodicity due to secondary MSP impacts, reducing macroscale undulation amplitude and thereby constraining *Sa* improvement.

Notably, the roughness disparity between composite processes intensified in extended sampling zones (3.0 × 3.0 mm^2), as evidenced by broader error margins in Fig. 4. This magnification arises from enhanced sensitivity to spot-overlap features at larger scales. For MSP-LSP specimens, the S-shaped laser trajectory interacted with pre-existing MSP indentations, amplifying roughness dispersion at overlap boundaries. Conversely, LSP-MSP specimens exhibited reduced *Sa* variability in extended zones, attributable to MSP-induced smoothing of laser-affected peripheries. These findings confirm that processing sequences govern roughness distribution through spatial reconfiguration of microstructural coupling mechanisms.

3.3 Influence of post-processing sequences on surface wettability

The contact angles of various specimens treated with different processes were quantitatively measured for test regions shown in Fig. 3. DSA-X optical contact angle measurements revealed significant wettability variations among differently processed

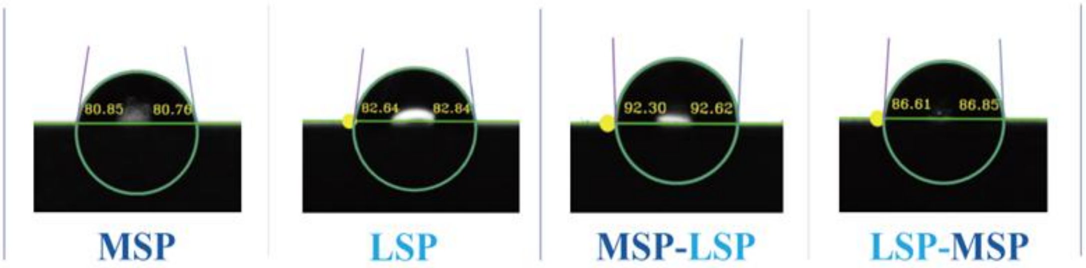

Fig. 5: Water droplet contact angle profiles on A100 steel surfaces.

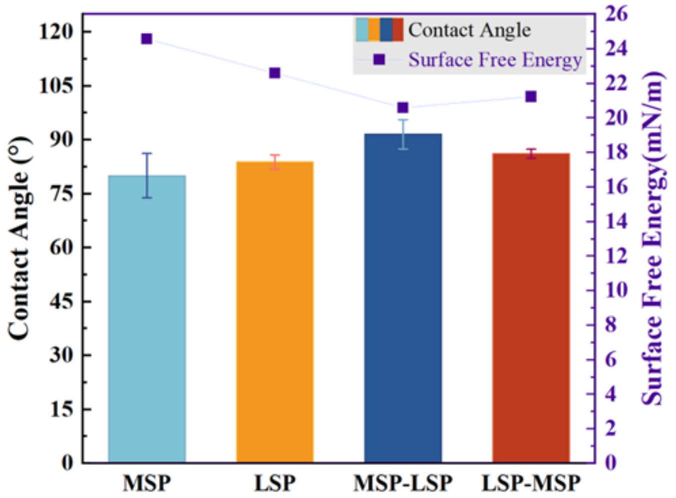

Fig. 6: Measured contact angles and surface energy for different treatment processes. The purple line indicates surface energy inversely correlated with contact angle.

A100 steel surfaces (Fig. 5). MSP-only treated specimens exhibited a contact angle of 80.03°, while LSP-only processing increased this value to 83.87°, demonstrating LSP's superior hydrophobicity enhancement. Notably, composite processes further amplified this trend: MSP-LSP sequential treatment achieved a contact angle of 91.58°, markedly exceeding the 86.14° observed for LSP-MSP. This established a hierarchical wettability order: $\theta_{\mathrm{MSP}} < \theta_{\mathrm{LSP}} < \theta_{\mathrm{LSP\text{-}MSP}} < \theta_{\mathrm{MSP\text{-}LSP}}$ (Fig. 6).

Correlating with the roughness analysis in Fig. 4, the MSP-LSP-treated surface achieved the highest roughness ($Sa = 1.62 \pm 0.04$ μm), characterized by multiscale features: periodic macrowaviness from LSP-induced pits superimposed with MSP-generated stochastic microroughness. This hierarchical architecture significantly increased the tortuosity of three-phase contact lines. According to the Cassie-Baxter wetting model, such structural coupling promotes a composite solid-liquid-air contact regime, effectively reducing the actual solid-liquid contact area and thereby enhancing hydrophobicity. In contrast, the LSP-MSP process partially degraded initial pit regularity through subsequent MSP impacts, diminishing macrowaviness amplitude ($Sa = 1.50 \pm 0.08$ μm) and weakening surface energy barriers. The surface energy profiles in Fig. 6 (purple polyline) further corroborated this mechanism. MSP-LSP specimens exhibited the lowest surface energy, consistent with their maximum contact angle, whereas MSP-only surfaces showed the highest surface energy indicative of hydrophilic behavior. Notably, despite LSP-MSP's superior residual compressive stress (Table 1), its moderate surface energy recovery revealed a competitive interplay between mechanical strengthening and wettability modification. The secondary MSP treatment enhanced mechanical performance at the expense of partial hydrophobicity loss, demonstrating process-sequence-dependent trade-offs.

3.4 Surface strengthening effects induced by post-processing sequences

This study focuses on the residual stress that is parallel to the surface of the target material. Residual stress measurements in Table 1 demonstrate that both single and composite processes introduced compressive residual stresses in A100 steel, with composite treatments exhibiting significantly superior strengthening. MSP-only and LSP-only specimens showed surface residual stresses of −964.39 ± 63.47 MPa and −860.83± 11.25 MPa, respectively. Composite processes

Table 1: Residual stress and FWHM of diffraction peaks.

	Residual stress (MPa)		FWHM (°)	
MSP	-964.39	±63.47	5.43	±0.10
LSP	-860.83	±11.25	4.81	±0.10
MSP-LSP	-1008.34	±22.18	5.07	±0.08
LSP-MSP	-1271.93	±10.92	5.61	±0.11

Note: The measurement values of both indicators and their inaccuracies have been statistically averaged.

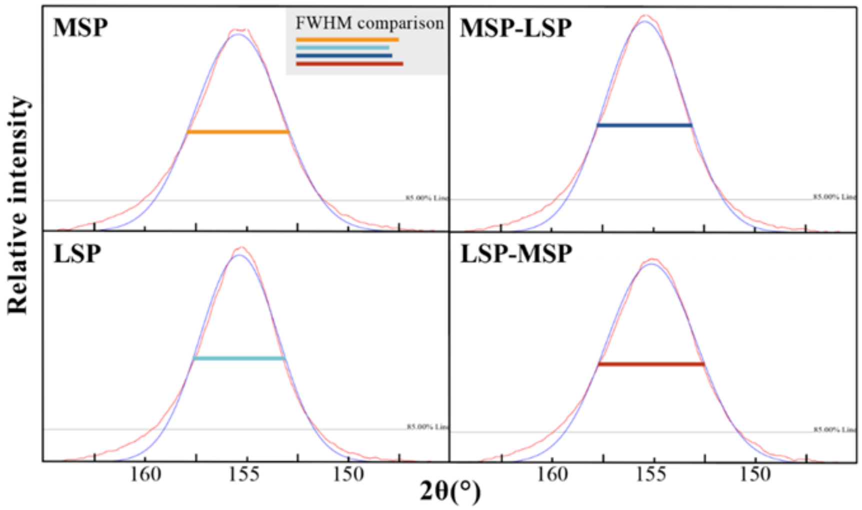

Fig. 7: X-ray diffraction patterns and FWHM analysis for different treatments. Peak broadening reflects grain refinement and lattice distortion.

elevated these values to −1008.34 ± 22.18 MPa (MSP-LSP) and −1271.93 ± 10.92 MPa (LSP-MSP), representing a maximum increase of 47.8% over single-process treatments. Notably, LSP-MSP generated substantially higher compressive stresses than MSP-LSP, attributable to cumulative work hardening mechanisms. In MSP-LSP sequencing, the pre-hardened layer from initial MSP treatment reduced stress transfer efficiency during subsequent LSP shockwaves. Conversely, LSP-MSP leveraged secondary MSP impacts to amplify residual stresses on LSP-pretreated surfaces, achieving synergistic stress accumulation through sequential work hardening.

X-ray diffraction patterns in Fig. 7 further elucidate the sequence-dependent microstructural evolution. The MSP-only specimen exhibited a diffraction peak full width at half maximum (FWHM) of 5.43 ± 0.10°, markedly exceeding the LSP-only value of 4.81 ± 0.10°, confirming MSP's superior efficacy in grain refinement and dislocation density enhancement. Among composite processes, LSP-MSP achieved the highest FWHM (5.61 ± 0.11°), surpassing MSP-LSP (5.07 ± 0.08°), demonstrating the dominant role of post-treatment in microstructural regulation. This sequence dependency originates from the pre-modified microstructures' influence on subsequent process responses: In LSP-MSP, secondary MSP impacts on LSP-pretreated substrates amplified lattice distortion through cumulative plastic deformation. Conversely, MSP-LSP's LSP stage was constrained by the limited plastic flow capacity of the pre-hardened MSP layer, restricting further defect generation.

In summary, the processing sequence governs the ultimate strengthening efficacy by modulating plastic deformation accumulation pathways. The LSP-MSP sequence achieves superior residual compressive stress through synergistic interaction between pre-strain (LSP-induced) and secondary impact (MSP-induced), whereas MSP-LSP exhibits constrained stress enhancement due to prior work hardening limiting subsequent LSP effectiveness. This mechanistic understanding establishes a critical theoretical foundation for optimizing composite process sequences to enhance tensile resistance in high-performance structural materials.

3.5 Strength characteristics of LSP-induced wavy morphology

Systematic comparisons between finite element simulations

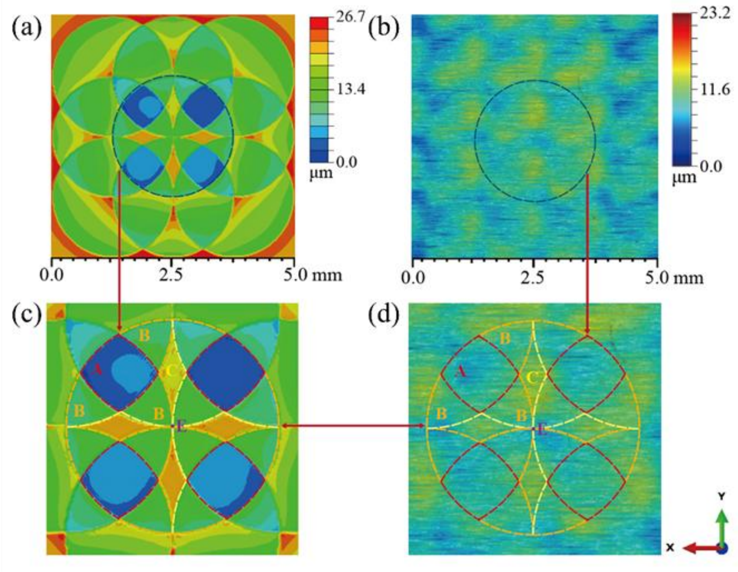

Fig. 8: Inhomogeneous distribution of surface undulation deformation in LSP-treated regions. (a) Surface height simulation; (b) Experimental surface morphology; (c) Comparison of simulated and experimental profiles of the central spot.

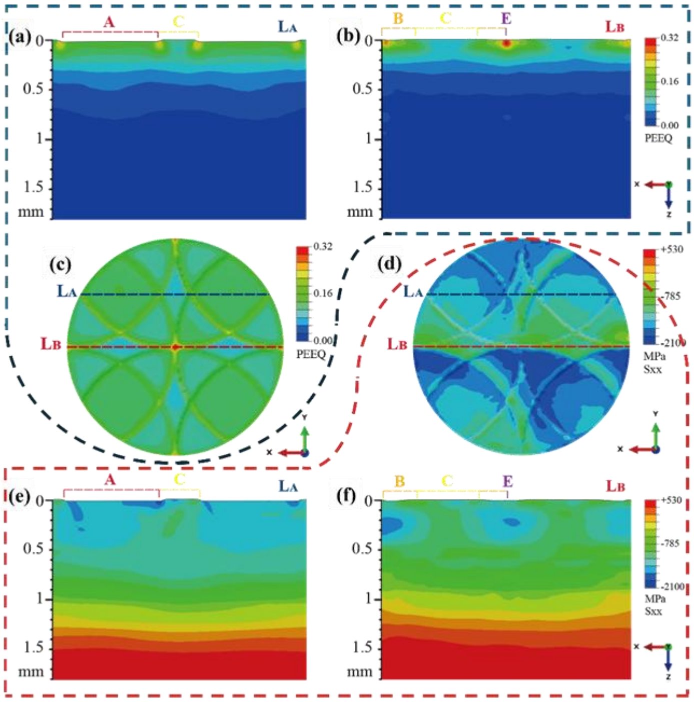

Fig. 9: *PEEQ* and residual stress (*S*xx) distribution across characteristic profiles (LA, LB). *S*xx refers to the residual stress parallel to the X-axis in the X0Y plane of the coordinate system as shown. (a-b) Cross-sectional analysis in *PEEQ*; (c) Surface distribution of *PEEQ*; (d) Surface distribution of residual stress (*S*xx); (e-f) Cross-sectional analysis in residual stress.

and experimental results (Fig. 8) revealed the mechanical essence of laser shock peening (LSP)-generated surface waviness. Fig. 8a displays the simulated surface height distribution, while Fig. 8b shows the experimentally observed morphology. Detailed spatial comparisons at central locations (Fig. 8(c-d)) demonstrate that LSP processing with 50% spot overlap generated periodic pit arrays with a minimum characteristic period of quarter-spot dimensions (1.25 × 1.25 mm^2). Notably, the simulation accurately replicated key morphological features in the laser-irradiated core region: A hierarchical pit architecture comprising Zone A (four overlapping spots), Zone B (three overlaps), and Zone C (two overlaps), with corresponding pit depths following gradient distribution (Zone A > B > C).

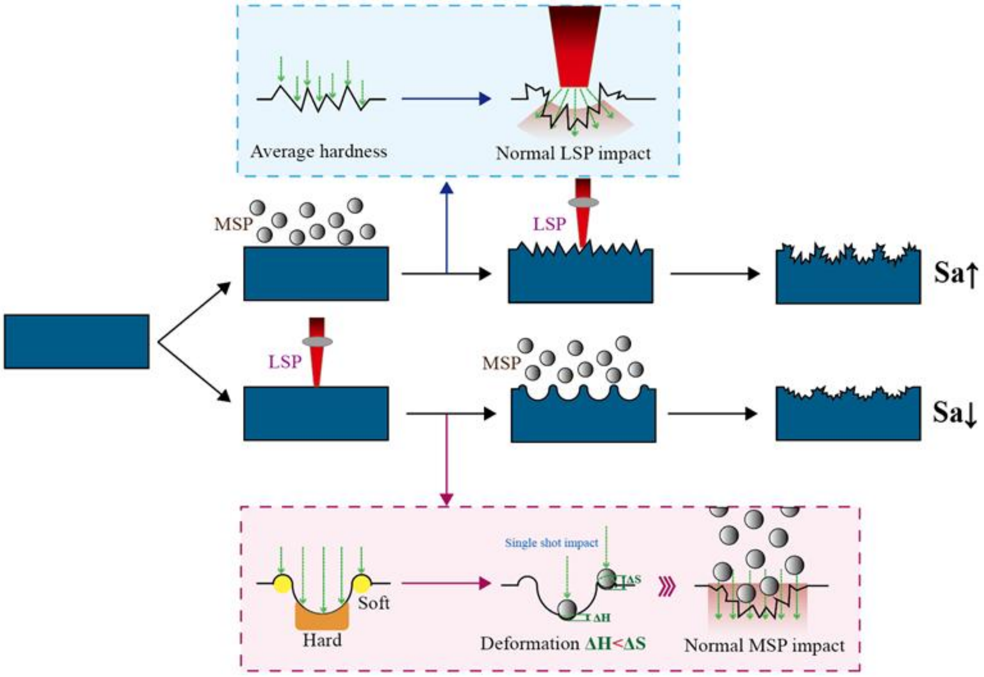

Fig. 10: Mechanism of surface roughness evolution under MSP-LSP and LSP-MSP.

Fig. 9 elucidates the correlation between surface morphology and mechanical properties through equivalent plastic strain (*PEEQ*) and residual stress (*S*xx) distributions. In the ABAQUS FE model, *PEEQ* quantifies cumulative plastic deformation, directly linked to laser-induced dislocation density and grain refinement. Simulation results (Fig. 9(a-c)) reveal that *PEEQ* values in Zone A (0.14) were twice those in Zone C (0.07), confirming a positive correlation between spot overlap frequency and plastic deformation severity. This distribution stems from energy superposition effects: overlapping regions experience higher energy densities, driving intensified plastic flow and deeper stress wave penetration. Notably, experimental observations of high dispersion at point E (four-spot overlap boundary) were attributed to minor deviations in practical spot path spacing. When actual spacing fell below theoretical values, increased overlap frequency deepened local depressions; conversely, larger spacing generated relative protrusions.

Residual stress profile analyses (Fig. 9(d-f)) revealed depth-dependent surface strengthening mechanisms. In the depression zone (Zone A), surface layers exhibited a residual compressive stress peak of −1200 MPa, decaying exponentially with depth, indicative of intense compressive plastic deformation induced by laser shockwaves. In contrast, protrusion zones (Zones B and C) showed maximum compressive stresses in subsurface layers, with distribution curves exhibiting an initial increase followed by a gradual reduction. This unique trend originates from stress redistribution caused by material lateral flow. The strong agreement between finite element simulations and experimental data (Fig. 8d) validated the model's reliability in predicting surface morphology evolution and mechanical responses.

Further mechanistic analysis demonstrated that the superior strengthening in depression zones stems from synergistic interactions between high *PEEQ* (0.14) and residual compressive stress (−1200 MPa). These regions experienced multi-impact-induced grain refinement (diffraction peak FWHM increased to 5.61°), dislocation density enhancement, and work hardening. Conversely, protrusion zones relied more on stress state rebalancing than plastic strain accumulation (*PEEQ* = 0.07), with subsurface-maximized residual stress distributions. This spatial heterogeneity between surface morphology and mechanical properties provides critical theoretical guidance for optimizing laser shock path design in achieving tailored performance gradients.

4. Discussion

4.1 Role of process sequence in surface morphology regulation

Systematic analysis of surface morphological characteristics under MSP-LSP and LSP-MSP composite processes (Fig. 3, 10) revealed that processing sequences critically influence final topography by regulating the superposition effects of microstructural evolution. Both sequences generated composite micro-nano structures on A100 steel surfaces, integrating MSP-induced disordered impact traces with LSP-

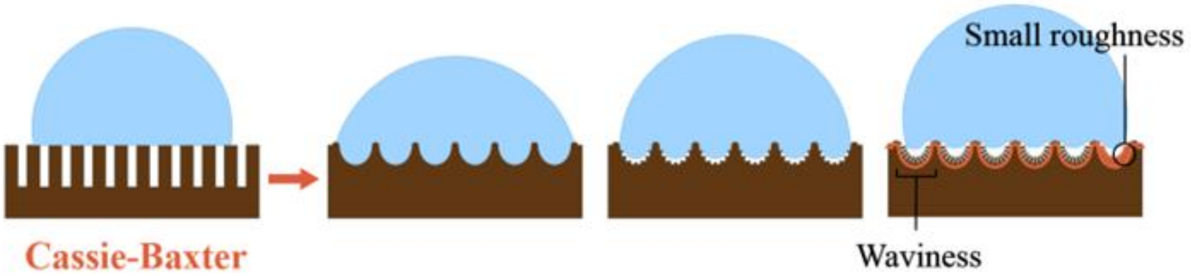

Fig. 11: Cassie-Baxter model for wettability on composite-processed surfaces. Air entrapment in hierarchical micro-nano structures enhances hydrophobicity.

derived periodic dimple features, yet exhibiting fundamentally distinct structural evolution pathways.

In the MSP-LSP sequence (Fig. 3(e-f)), the homogenized micro-roughness substrate formed by the initial MSP process provided a stable stress-transfer medium for subsequent LSP. This enabled complete reconstruction of periodic dimple structures via laser shockwaves, amplifying macroscopic waviness amplitude while enhancing the spatial frequency of microscopic roughness, ultimately yielding a high-roughness surface (Fig. 4). In contrast, the LSP-MSP sequence (Fig. 3g-h) exhibited significant structural degradation due to dynamic modification of initial dimples by secondary MSP. Comparative analysis of impact-response mechanisms (Fig. 10) demonstrated heterogeneous deformation between pre-LSP-generated depression zones (residual compressive stress: −1200 MPa) and protrusion zones (−850 MPa) during subsequent MSP: the high-strength depression zones restricted projectile penetration depth, whereas low-stress protrusion zones permitted extensive plastic deformation. This non-uniform deformation partially disrupted dimple periodicity, reducing macroscopic waviness amplitude and increasing microscopic roughness dispersion, ultimately forming a moderately rough surface ($Sa = 1.50 \pm 0.08$ μm).

Experimental and simulation results jointly confirm that process sequences achieve precise regulation of hierarchical surface characteristics (waviness/roughness transition thresholds) and distribution homogeneity by modulating spatial coupling modes of microstructural evolution. The MSP-LSP sequence prioritizes structural integrity preservation through sequential energy superposition, while LSP-MSP leverages stress-gradient-driven selective deformation for performance customization. This mechanistic understanding establishes process sequence as a programmable design parameter for multifunctional surface engineering.

4.2 Wettability model under process sequence influence

Systematic comparisons of surface roughness and wettability characteristics across different process sequences (Fig. (5-6)) revealed a hierarchical roughness relationship: $Sa_{\mathrm{MSP}} < Sa_{\mathrm{LSP}} < Sa_{\mathrm{LSP\text{-}MSP}} < Sa_{\mathrm{MSP\text{-}LSP}}$, with corresponding contact angle gradients following $\theta_{\mathrm{MSP}} < \theta_{\mathrm{LSP}} < \theta_{\mathrm{LSP\text{-}MSP}} < \theta_{\mathrm{MSP\text{-}LSP}}$. This demonstrates a positive correlation between surface roughness and hydrophobicity within the studied process window, where increased roughness enhances contact angles and reduces wettability.

The wettability mechanism was interpreted through the Cassie-Baxter model (Fig. 11). Composite-processed surfaces integrate LSP-generated periodic macroscale dimples (characteristic length ~1.25 mm) with MSP-induced disordered microscale impact craters (~0.6 mm), forming a dual-scale hierarchical architecture of macroscopic waviness and microscopic roughness. Upon liquid contact, air pockets trapped within these multiscale structures establish solid-liquid-gas triphasic interfaces, minimizing the actual solid-liquid contact area. According to theory,[29,30] the apparent contact angle (θ_{CB}) relates to the roughness factor and gas fraction as Eq. (1):

$$cos\theta_{\mathrm{CB}} = r\phi cos\theta_{\mathrm{Y}} - (1-\phi) \qquad (1)$$

where r (roughness factor, actual/projected area ratio) quantifies surface topography amplification, and ϕ (gas fraction) represents air-trapped area proportion. The term $r\phi\cos\theta_{\mathrm{Y}}$ amplifies intrinsic wettability, while $(1-\phi)$ penalizes direct liquid-solid contact.

The MSP-LSP sequence synergistically amplified macroscopic waviness (increasing r) and microscopic roughness (reducing φ), elevating the apparent contact angle from 80.03° (MSP-only) to 91.58°, approaching the hydrophobic threshold. Critically, process sequences modulated wettability by governing the spatial coupling of hierarchical structures. In MSP-LSP, the uniform micro-roughness substrate ($Sa = 0.81$ μm) formed by initial MSP stabilized stress wave propagation, enabling full retention and additive amplification of periodic dimples (ΔSa ~0.81 μm). Conversely, LSP-MSP suffered reduced macroscopic

Table 2: Surface properties under different process sequences.

Process Sequence	Residual Stress (MPa)	Strengthening Effect	Roughness (*Sa*, μm)	Undulation Degree	Contact Angle (°)	Hydrophobicity
MSP-LSP	-1008.34±22.18	Poor	1.62±0.04	High	91.58±4.05°	Good
LSP-MSP	-1271.93±10.92	Good	1.50±0.08	Low	86.14±1.26°	Poor

waviness amplitude (ΔSa ~0.32 μm) and increased φ due to MSP-induced randomization of initial dimples (Fig. 3(g-h)), limiting contact angle enhancement.

Experimental-model consistency validated quantitative correlations between morphological parameters (r, φ) and wettability, establishing process sequence optimization as a theoretical foundation for precision wettability regulation. The MSP-LSP sequence maximizes Cassie-Baxter state stability by coupling multiscale structural integrity, whereas LSP-MSP highlights the antagonistic effects of sequential mechanical-thermal interactions on functional performance. These insights advance the rational design of multifunctional surfaces through programmable process-sequence engineering.

4.3 Mechanism of process sequence effects on dual-functional modification

Integrated analysis of Table 2 data and morphological characteristics (Fig. 3, 10) reveals distinct sequence-dependent regulation of surface performance. Experimental results demonstrate that MSP-LSP and LSP-MSP sequences exhibit significant differences in mechanical strengthening and wettability: MSP-LSP-treated specimens achieved residual compressive stresses of −1008.34 ± 22.18 MPa and a contact angle of 91.58 ± 4.05°, with surface roughness reaching 1.62 ± 0.04 μm and prominent multiscale undulating features. In contrast, LSP-MSP specimens exhibited higher residual compressive stresses (−1271.93 ± 10.92 MPa) but lower roughness (1.50 ± 0.08 μm) and contact angle (86.14 ± 1.26°). These performance divergences arise from sequence-governed spatial coupling mechanisms during microstructural evolution.

The LSP-MSP sequence enhanced mechanical performance through a synergistic “pre-strain and secondary impact” pathway. As schematically illustrated in Fig. 10, heterogeneous plastic deformation occurred between pre-LSP-generated depression zones (residual stress: −1200 MPa) and protrusion zones (−850 MPa) during subsequent MSP. Stress-gradient-driven heterogeneous deformation behavior emerged: high-strength depressions restricted projectile penetration depth, while low-stress protrusions permitted extensive plastic flow. This spatial stress superposition amplified residual compressive stresses, achieving a 47.8% enhancement compared to single processes. Such stress intensification renders LSP-MSP ideal for tensile-critical components like aeroengine blades.

The MSP-LSP sequence employed a “substrate homogenization and waviness construction” strategy. On an MSP-preconditioned uniform micro-roughness substrate (Sa = 0.81 μm), subsequent LSP superimposed periodic dimples (ΔSa~0.81 μm), forming a multiscale architecture (Fig. 3(e-f)). This hierarchical structure synergistically amplified roughness features (macro-waviness and micro-roughness), increasing the roughness factor (r) and reducing gas fraction (φ) per the Cassie-Baxter model. These effects elevated the contact angle from 80.03° (MSP-only) to 91.58°, approaching hydrophobicity. Such performance positions MSP-LSP as optimal for anti-icing applications in extreme environments, such as Arctic aerospace components.

Further analysis revealed three interlinked mechanisms governing sequence-dependent surface modification: (1) Preconditioning Regulation: Initial treatments (MSP/LSP) modulate subsequent process responses by altering surface states (hardness gradients, residual stress distributions); (2) Stress Wave Redirection: Process sequences differentially guide stress wave propagation and plastic strain accumulation. For example, LSP-MSP leverages stress-gradient-driven secondary superposition; (3) Spatiotemporal Coupling: Hierarchical microstructures (Fig. 3) interact with mechanical states (*e.g.*, compressive stress fields) to enable performance customization.

This mechanistic framework establishes a dual-objective optimization strategy: MSP-LSP prioritizes hydrophobicity, while LSP-MSP maximizes mechanical strengthening. The results demonstrate the viability of process sequence engineering for resolving functional-strength trade-offs in aerospace surface modification.

5. Conclusion

This study systematically elucidates the regulation mechanisms of MSP/LSP composite process sequences on the “wettability-strengthening” duality in A100 ultrahigh-strength steel, yielding the following key conclusions:

(1) Sequential Construction of Multiscale Architectures

Composite processes construct hierarchical architectures with dual macro-micro characteristics. The MSP-LSP sequence preserves intact periodic dimple structures due to stress-transfer advantages from the homogenized MSP-pretreated substrate, achieving 8% higher surface roughness than LSP-MSP. This sequence amplifies synergistic interactions between waviness and roughness through coherent structural coupling.

(2) Process-Sequence-Dependent Wettability

Wettability strictly adheres to the Cassie-Baxter model, where multiscale structures enhance hydrophobicity by increasing three-phase contact line tortuosity. The spatial coupling intensity between macrowaviness and microroughness governs wettability, with process sequence directly modulating gas fraction (φ) and roughness factor (r) via hierarchical integrity control.

(3) Synergistic Strengthening in Composite Processes

Composite treatments elevate surface residual compressive stresses by up to 47.8% compared to single processes. LSP-MSP outperforms MSP-LSP in stress amplification due to stress-gradient-enhanced secondary hardening, where pre-LSP-induced stress heterogeneities optimize subsequent MSP-driven plasticity accumulation.

(4) "Functionality-Strengthening" Co-Regulation Mechanism

Process sequences enable precision performance customization: LSP-MSP achieves 31.9% residual stress enhancement for tensile-critical components (*e.g.*, aeroengine blades), while MSP-LSP prioritizes anti-icing functionality with a 14.5% contact angle increase. This dual-objective optimization framework resolves long-standing trade-offs in multifunctional surface engineering.

Acknowledgments

This work was supported by the National Natural Science Foundation of China (52171073, 52075298, 51801031), the National Key R&D Program of China (GLAM: 2023YFE0106500), the Taishan Scholars Program (tsqn202312299), and the Xiaomi Young Talents Program (2024XM05). The work described was carried out as part of the GLAM (SINO-MALTA-2022-13) project which was financed by XJENZA Malta and the Ministry for Science and Technology of the People's Republic of China (MOST), through the SINO-MALTA Fund 2022 (Science and Technology Cooperation).

Conflict of Interest

The authors declare no conflict of interest.

Supporting Information

Not applicable.

CRediT Statement

Guoxin Lu: Writing - Review & editing, Writing - Original draft, Methodology, Investigation, Funding acquisition, Formal analysis, Data curation, Conceptualization, **Di Zhao:** Writing - Original draft, Methodology, Investigation, Conceptualization, **Qiang Wang:** Resources, Investigation, **Zhong Ji:** Writing - Review & editing, Resources, Investigation, **Zhong Chen:** Writing - Review & editing, Investigation.

References

[1] S. Kikuchi, K. Minamizawa, J. Arakawa, H. Akebono, S. Takesue, M. Hayakawa, Combined effect of surface morphology and residual stress induced by fine particle and shot peening on the fatigue limit for carburized steels, *International Journal of Fatigue*, 2023, **168**, 107441, doi: 10.1016/j.ijfatigue.2022.107441.

[2] C. Zhang, Y. Dong, C. Ye, Recent developments and novel applications of laser shock peening: a review, *Advanced Engineering Materials*, 2021, **23**, 2001216, doi: 10.1002/adem.202001216.

[3] P. Roshith, The influence of compressive residual stress on metallurgical and mechanical properties of materials exposed to shot peening: a review, *Canadian Metallurgical Quarterly*, 2024, **63**, 373-413, doi: 10.1080/00084433.2023.2213045.

[4] W. Okuniewski, M. Walczak, M. Szala, D. Chocyk, Effect of surface modification by shot peening on cavitation erosion resistance of titanium alloy Ti-6Al-4V produced by DMLS method, *Engineering Failure Analysis*, 2025, **176**, 109653, doi: 10.1016/j.engfailanal.2025.109653.

[5] K. Praveenkumar, S. Sudhagara Rajan, S. Swaroop, G. Manivasagam, Laser shock peening: a promising tool for enhancing the aeroengine materials' surface properties, *Surface Engineering*, 2023, **39**, 245-274, doi: 10.1080/02670844.2023.2206186.

[6] A. Kishore, M. John, A. M. Ralls, S. A. Jose, U. B. Kuruveri, P. L. Menezes, Ultrasonic nanocrystal surface modification: processes, characterization, properties, and applications, *Nanomaterials*, 2022, **12**, 1415, doi: 10.3390/nano12091415.

[7] K. Tserpes, P. Kormpos, Detailed finite element models for the simulation of the laser shock wave response of 3D woven composites, *Journal of Composites Science*, 2024, **8**, 83, doi: 10.3390/jcs8030083.

[8] A. Behvar, M. Haghshenas, A critical review on very high cycle corrosion fatigue: Mechanisms, methods, materials, and models, *Journal of Space Safety Engineering*, 2023, **10**, 284-323, doi: 10.1016/j.jsse.2023.05.002.

[9] Z. Jie, Z. Zhang, L. Susmel, L. Zhang, W. Lu, Corrosion fatigue mechanisms and evaluation methods of high-strength

steel wires: a state-of-the-art review, *Fatigue & Fracture of Engineering Materials & Structures*, 2024, **47**, 2287-2318, doi: 10.1111/ffe.14311.

[10] D. Zhao, G. Lu, Y. Yao, B. Attard, X. Luo, Z. Ji, Regulating material wettability through surface plastic deformation post-processing *via* friction modification, *Tribology International*, 2024, **198**, 109901, doi: 10.1016/j.triboint.2024.109901.

[11] S. Abbasi, M. Nouri, A. S. Rouhaghdam, An investigation of the wettability and chemical stability of superhydrophobic coatings on titanium, *Thin Solid Films*, 2022, **762**, 139541, doi: 10.1016/j.tsf.2022.139541.

[12] S. Yu, C. Ning, H. Wu, Z. Li, Y. Wu, Z. Cai, Comparison of surface integrity, microstructure and corrosion resistance of Zr-4 alloy with various laser shock peening treatments, *Surface and Coatings Technology*, 2025, **498**, 131799, doi: 10.1016/j.surfcoat.2025.131799.

[13] Z. Qin, B. Li, X. Huang, H. Zhang, R. Chen, M. Adeel, H. Xue, The effect of laser shock peening on surface integrity and high and very high cycle fatigue properties of 2024-T351 aluminum alloy, *Optics & Laser Technology*, 2022, **149**, 107897, doi: 10.1016/j.optlastec.2022.107897.

[14] X. Luo, N. Dang, X. Wang, The effect of laser shock peening, shot peening and their combination on the microstructure and fatigue properties of Ti-6Al-4V titanium alloy, *International Journal of Fatigue*, 2021, **153**, 106465, doi: 10.1016/j.ijfatigue.2021.106465.

[15] Y. Gou, J. Zhou, L. Li, P. Li, X. Meng, S. Huang, Laser peening without coating fabricated superhydrophobic aluminum alloy with favorable mechanical properties, *Materials Today Communications*, 2024, **39**, 108616, doi: 10.1016/j.mtcomm.2024.108616.

[16] M. A. Zaman, S. Wang, Experimental investigation of surface roughness/wettability pattern effect on crystallization fouling over falling-film flow, *Desalination*, 2024, **575**, 117324, doi: 10.1016/j.desal.2024.117324.

[17] H. U. Sajid, R. Kiran, Influence of corrosion and surface roughness on wettability of ASTM A36 steels, *Journal of Constructional Steel Research*, 2018, **144**, 310-326, doi: 10.1016/j.jcsr.2018.01.023.

[18] S. Lu, J. Sun, Y. Ma, N. Sun, Pre-mixed abrasive waterjet peening with post-low stress milling process and the effect of process parameters on the surface integrity of TC11 titanium alloy, *Surface and Coatings Technology*, 2024, **478**, 130409, doi: 10.1016/j.surfcoat.2024.130409.

[19] Y. Yin, Y. Shang, W. He, C. Wang, L. Zhou, Improving the fretting fatigue properties of Ti-6Al-4V dovetail joint treated by laser shock peening and shot peening, *International Journal of Fatigue*, 2025, **198**, 108996, doi: 10.1016/j.ijfatigue.2025.108996.

[20] Z. Zhang, W. Qiu, G. Zhang, D. Liu, P. Wang, Progress in applications of shockwave induced by short pulsed laser on surface processing, *Optics & Laser Technology*, 2023, **157**, 108760, doi: 10.1016/j.optlastec.2022.108760.

[21] P. Peyre, R. Fabbro, Laser shock processing: a review of the physics and applications, *Optical and Quantum Electronics*, 1995, **27**, 1213-1229, doi: 10.1007/BF00326477.

[22] R. Pan, M. Cai, W. Liu, X. Luo, C. Chen, H. Zhang, M. Zhong, Extremely high Cassie–Baxter state stability of superhydrophobic surfaces *via* precisely tunable dual-scale and triple-scale micro–nano structures, *Journal of Materials Chemistry A*, 2019, **7**, 18050-18062, doi: 10.1039/C9TA04484A.

[23] L. Wang, Z. Tian, G. Jiang, X. Luo, C. Chen, X. Hu, H. Zhang, M. Zhong, Spontaneous dewetting transitions of droplets during icing & melting cycle, *Nature Communications*, 2022, **13**, 378, doi: 10.1038/s41467-022-28036-x.

[24] Y. Liao, F. Rubbi, B. Mao, B. Li, F. Delzendehrooy, M. M. Haque, A novel solid-state metal additive manufacturing process–Laser-induced Supersonic Impact Printing (LISIP): Exploration of process capability, *Additive Manufacturing*, 2024, **93**, 104356, doi: 10.1016/j.addma.2024.104356.

[25] G. Z. Sakhvadze, Features of finite element simulation of laser impact welding of aluminum with stainless steel, *Journal of Machinery Manufacture and Reliability*, 2024, **53**, 351-359, doi: 10.1134/S1052618824700183.

[26] X. Wang, F. Li, T. Huang, X. Wang, H. Liu, Experimental and numerical study on the laser shock welding of aluminum to stainless steel, *Optics and Lasers in Engineering*, 2019, **115**, 74-85, doi: 10.1016/j.optlaseng.2018.11.012.

[27] R. Fabbro, J. Fournier, P. Ballard, D. Devaux, J. Virmont, Physical study of laser-produced plasma in confined geometry, *Journal of Applied Physics*, 1990, **68**, 775-784, doi: 10.1063/1.346783.

[28] Y. Hu, Z. Yao, J. Hu, 3-D FEM simulation of laser shock processing, *Surface and Coatings Technology*, 2006, **201**, 1426-1435, doi: 10.1016/j.surfcoat.2006.02.018.

[29] A. Marmur, The lotus effect: superhydrophobicity and metastability, *Langmuir*, 2004, **20**, 3517-3519, doi: 10.1021/la036369u.

[30] D. Quéré, Wetting and roughness, *Annual Review of Materials Research*, 2008, **38**, 71-99, doi: 10.1146/annurev.matsci.38.060407.132434.

Open Access